DOI: 10.1002/cssc.201300742

Hierarchical Sulfur-Based Cathode Materials with Long Cycle Life for Rechargeable Lithium Batteries

Jiulin Wang,*[a] Lichao Yin,[a] Hao Jia,[a] Haitao Yu,[a] Yushi He,[a] Jun Yang,[a] and Charles W. Monroe[b]

Composite materials of porous pyrolyzed polyacrylonitrile–sulfur@graphene nanosheet (pPAN–S@GNS) are fabricated through a bottom-up strategy. Microspherical particles are formed by spray drying of a mixed aqueous colloid of PAN nanoparticles and graphene nanosheets, followed by a simple heat treatment with elemental sulfur. The pPAN–S primary nanoparticles are wrapped homogeneously and loosely within a three-dimensional network of graphene nanosheets (GNS). The hierarchical pPAN–S@GNS composite shows a high reversible capacity of 1449.3 $mAh\,g^{-1}_{sulfur}$ or 681.2 $mAh\,g^{-1}_{composite}$ in the second cycle; after 300 cycles at a 0.2 C charge/discharge rate the capacity retention is 88.8% of its initial reversible value. Additionally, the coulombic efficiency (CE) during cycling is near 100%, apart from in the first cycle, in which CE is 81.1%. A remarkable capacity of near 700 $mAh\,g^{-1}_{sulfur}$ is obtained, even at a high discharge rate of 10 C. The superior performance of pPAN–S@GNS is ascribed to the spherical secondary GNS structure that creates an electronically conductive 3D framework and also reinforces structural stability.

Introduction

Owing to their near-universal adoption as power sources for consumer electronics, traditional rechargeable lithium-ion batteries are finding many alternative uses.[1] But the energy densities and power densities of rechargeable Li-ion batteries must be increased for transportation applications, and their cycle lives must be lengthened for applications in the utility grid. To reach these more stringent performance goals, much research has focused on the development of new electrode materials and the design of new electrode microstructures.[2]

Elemental sulfur (S_8) is one of the most promising new cathode materials for next-generation rechargeable lithium batteries, primarily because of its high theoretical specific capacity, 1672 $mAh\,g^{-1}$ (relative to a metallic Li anode, this corresponds to an energy density of 2.6 $Wh\,kg^{-1}$[3]). Sulfur has other advantages, such as low cost and low environmental impact. Several challenges prevent the widespread adoption of sulfur cathodes, however. Sulfur has low electrical conductivity and undergoes extreme volume expansion during cycling; as the charge state of the electrode varies, polysulfides can sometimes dissolve into the electrolyte phase, facilitating undesired side reactions, capacity loss, and poor charge/discharge efficiencies as a result of sulfur shuttling.[4] Because of these problems, state-of-the-art sulfur cathodes have relatively small specific capacities, poor cycle lives, and low coulombic efficiencies. A promising route to address these challenges is to produce sulfur-based composites. A hierarchical, composite structure can be used to achieve high electrical conductivity in the sulfur-supporting matrix, as well as giving it an inherent sulfur-locking function.

Conductive supporting materials for sulfur cathodes include nanoporous or nanosheet carbon matrices,[5] conducting polymers,[6] and pyrolyzed polyacrylonitrile (pPAN).[7] Surface wrapping by conductive polymers or nanoparticles has also been reported as an effective strategy to suppress polysulfide dissolution.[8] Recently, TiO_2 shell was reported to clearly stabilize the cycling of Li/S battery.[8c]

Our previous research suggests that pPAN–S composites enhance both rate capability and stability under cycling, especially after in situ polymerization is used to introduce additional electrically conductive material into the composite; the PAN nano particles were anchored on the GNS surface, and the special structure was maintained in the subsequent vulcanization process.[9] This approach is still far from practical adoption owing to the harsh polymerization conditions required. In addition, nanostructured electrodes have extremely high surface-to-volume ratios that could potentially cause serious interface reactions with the electrolyte and possibly complicate the procedure to prepare electrodes. Therefore, new and facile strategies to prepare microspheres are essential to improve the electrochemical performances of sulfur cathodes and accelerate their practical application.

Spray drying is widely used for nanoparticle encapsulation in the chemical engineering and food industries because of its

[a] Prof. J. Wang, Dr. L. Yin, H. Jia, H. Yu, Dr. Y. He, Prof. J. Yang
Department of Chemical Engineering
Shanghai Jiao Tong University
Shanghai 200240 (PR China)
E-mail: wangjiulin@sjtu.edu.cn

[b] Prof. C. W. Monroe
Department of Chemical Engineering
University of Michigan
Ann Arbor, MI 48109 (USA)

Supporting Information for this article is available on the WWW under http://dx.doi.org/10.1002/cssc.201300742.

low cost, simple apparatus, and easy scale-up property. Capillary compression can be used to convert two-dimensional (2D) graphene oxide (GO) sheets into 3D crumpled or flexible graphene particles. As a result of the large capillary forces involved, spray drying is, in principle, suitable for preparing 3D graphene composites.[10] To achieve regular hierarchical structures by means of spray drying, it is necessary that all the precursors remain homogeneously mixed throughout the drying process. Fortunately, chemically converted graphene nanosheets (GNS) obtained from graphene oxide can readily form stable, homogeneous aqueous colloids through electrostatic stabilization.[11] Also, mono-dispersed PAN nanoparticles can be prepared by dispersion/emulsion polymerization of acrylonitrile in a continuous aqueous phase.[12] This paper presents a straightforward strategy for synthesizing graphene-wrapped pPAN–S composite cathode materials and investigates their electrochemical performances in rechargeable Li–S batteries.

Results and Discussion

Formation of hierarchical pPAN–S@GNS microspheres

Scheme 1 shows an overview of the typical synthesis procedure used to form composite materials. The procedure begins

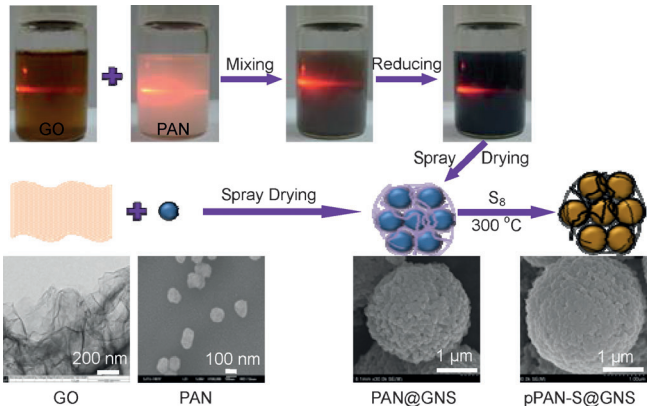

Scheme 1. Schematic illustration of the synthesis process, including production of the spherical nanoporous PAN@GNS precursor material and pyrolysis to form the pPAN–S@GNS composite. Observed Tyndall effects confirm the colloidal natures of the dispersions.

with the mixing of aqueous dispersions of GO nanosheets and PAN nanoparticles; after spray drying of this dispersion to form a PAN@GNS precursor material, the resulting particles are pyrolyzed in the presence of elemental sulfur to produce the pPAN–S@GNS composite. More details are provided in the Experimental Section.

Monodisperse PAN nanoparticles were prepared by dispersion/emulsion polymerization of acrylonitrile in a continuous aqueous phase supported by alkyl-sulfate surfactants, in the presence of a potassium persulfate initiator. The nanoparticle size can be easily adjusted by controlling reaction parameters such as monomer concentration, types and concentrations of initiator and surfactant, polymerization temperature, and time. In comparison to commercialized PAN, which is significantly randomly aggregated and therefore polydisperse, the PAN nanoparticles prepared in this work had relatively uniform size and form a stable colloid in the aqueous solution, as shown in Scheme 1 and supplementary Figure S1.

The PAN colloid was mixed with a GO dispersion and GO was subsequently reduced by hydrazine hydrate to GNS. The as-prepared GNS remained stable as a colloid (similar to its precursor GO) after ammonia was added to adjust its surface charge density. The stability is illustrated in Scheme 1; a photograph demonstrating the stability of the colloidal solution is shown in Figure S2.[11]

After the PAN and GO precursors were prepared and mixed, hierarchically structured PAN@GNS particles were readily produced through spray drying of the mixture. To obtain an electronically conductive composite, PAN nanoparticles and GNS were homogeneously mixed during spray drying to ensure that almost every PAN nanoparticle was loosely wrapped by crumpled GNS. After drying, the precursor was further treated with elemental sulfur at 300 °C to obtain the pPAN–S@GNS composite (sample A).

A typical SEM image of the composite material is shown in Figure 1 a. The image shows that the pPAN–S@GNS comprises secondary spherical microparticles, with diameters ranging from 1–5 μm. Observed at a high magnification (Figure 1 b), each microsphere is actually seen to be a tight aggregate of primary pPAN–S particles, which all have similar diameters of approximately 0.1 μm. The incorporation of sulfur seems to have minimal effect on the PAN morphology and only induces

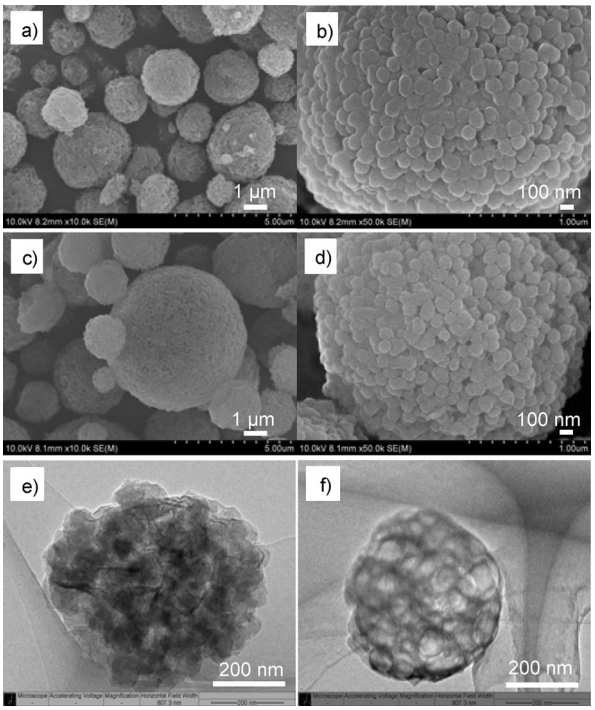

Figure 1. SEM images of a, b) the pPAN–S@GNS composite (sample A) and c, d) the PAN@GNS precursor synthesized by spray drying; TEM images of e) the PAN@GNS and f) the residual 3D graphene framework that remains after dissolution of PAN by DMF.

a small expansion of the nanoparticles (from 90 to 100 nm in diameter), suggesting that pPAN–S@GNS inherits its precursor's special hierarchical structure (Figure 1 c and d). TEM images of individual PAN@GNS microspheres (Figure 1 e) demonstrate that the PAN nanoparticles are uniformly wrapped by graphene nanosheets. To illustrate the graphene distribution in the composite more clearly, PAN was dissolved by treating the PAN@GNS with *N*,*N*-dimethylformamide (DMF) solvent. As expected, the foam-like residual comprises a spherical 3D graphene network, as illustrated in Figure 1 f. Figure 2 provides side-by-side SEM and EDS measurements to show that sulfur is uniformly distributed in the pPAN–S@GNS composite.

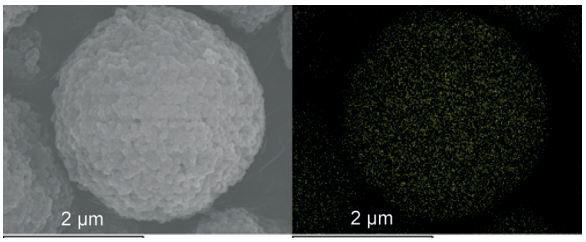

Figure 2. Sulfur distribution (yellow points, right) in the pPAN–S@GNS composite analyzed by comparison of SEM (left) and EDS images.

Two other sulfur-containing composites were prepared for comparison to sample A. Sample B was synthesized by a similar procedure to that outlined above, except commercial, polydisperse PAN was used. Sample C was prepared by conventional heat drying of the mixed suspensions of monodisperse PAN nanoparticles and GO.

Sample B had a secondary microspherical morphology, but the primary pPAN–S particles were randomly aggregated (see Figure S3 a and b); TEM images showed poor contact between pPAN–S and GNS (Figure S4). The significant aggregation inherent in the commercial PAN appears to be difficult to break down by re-dispersion in water. During the spray-drying process, liquid drops shrink in an irregular manner because of the unordered size of the PAN particles, leading to very loose structures in the dried microspheres.

For sample C, the secondary structure was barely visible in the composite product. Instead, domains with a relatively high accumulation of pPAN–S particles or GNS were observed (Figure S3 c, d).

The results of different synthesis strategies strongly indicate that the monodispersity of the PAN nanoparticles and homogeneous suspension of the GNS, as well as the manner of drying used to form the PAN@GNS precursor, are key to controlling the ultimate hierarchically structured composite material. Hierarchical microspheres containing PAN nanoparticles homogeneously wrapped in GNS were only obtained through spray drying an initial colloidal dispersion.

For syntheses following the procedure in Scheme 1, XRD was employed to illustrate the structural evolution of precursors as they formed the final product (Figure S5). The change of diffraction peaks between graphene and GO patterns indicates that the interlayer spacing of the GO is much larger than that of pristine graphite owing to the presence of functional groups on the graphitic sheets. Figure S5 c shows the XRD pattern of a PAN@GNS precursor prepared by spray drying. The GO peak at 10.9° is absent in the PAN@GNS composite; only the typical reflection at 16.8° for PAN and a weak GNS peak at 26° are observed (Figure S5d), indicating that the layer-stacking regularity almost disappears after spray drying. For a pPAN–S/GNS composite containing approximately 47 wt% S and approximately 5 wt% GNS, the characteristic peaks associated with crystalline sulfur are not detectable (Figure S5 b), except for a broad peak around 25° (Figure S5 a). This suggests that sulfur becomes amorphous and homogeneously distributed in the pyrolyzed PAN matrix during synthesis. Detailed information about the reactions that take place to form pPAN–S have been explored and discussed in previous papers by the authors.[7a]

Electrochemical performances

Measurements of pPAN–S and pPAN–S@GNS surface areas using the BET isotherm (Table 1) indicate that a considerable void space exists between the PAN nanoparticles and the GNS in the composite. Void space in secondary structures may effectively accommodate the volume changes of pPAN–S during cycling and also ensure penetration of electrolyte into the pPAN–S@GNS microparticles. Moreover, the composite's conductivity approaches 31 $mS\,cm^{-1}$ with GNS addition.

Table 1. Physical properties of the samples.

Sample	D: pPAN–S	A: pPAN–S@GNS
surface area [$m^2\,g^{-1}$]	15.36	31.91
pore diameter [nm]	–	40.5
pore volume [$cm^3\,g^{-1}$]	0.081	0.267
conductivity [$mS\,cm^{-1}$]	0.53	31

Composite samples A, B, and C were assembled into coin cells to evaluate their electrochemical performances. For comparison, a pPAN–S composite without GNS (sample D) using dispersed PAN nanoparticles as a precursor was also prepared. The sulfur content of the pPAN–S composite strongly affects its specific capacity: the higher the sulfur content, the larger the capacity of the composite. Higher sulfur content can, however, lead to the formation of a layer of elemental sulfur on the surface of the composite particles, particularly above 50 wt%, causing performance to deteriorate over many cycles.[9] Previous work suggests that 40–47 wt% sulfur provides an optimal balance of high capacity and cycling stability in pPAN–S composites.

Figure 3 a shows that the basic electrochemical characteristics of sample A are typical of pPAN–S composite cathode materials: unusually low lithiation potential in the first cycle and sloped charge/discharge curves in subsequent cycling. These features indicate that the GNS in the composite formed by spray drying does not significantly disturb the behavior of combined PAN and sulfur.[9]

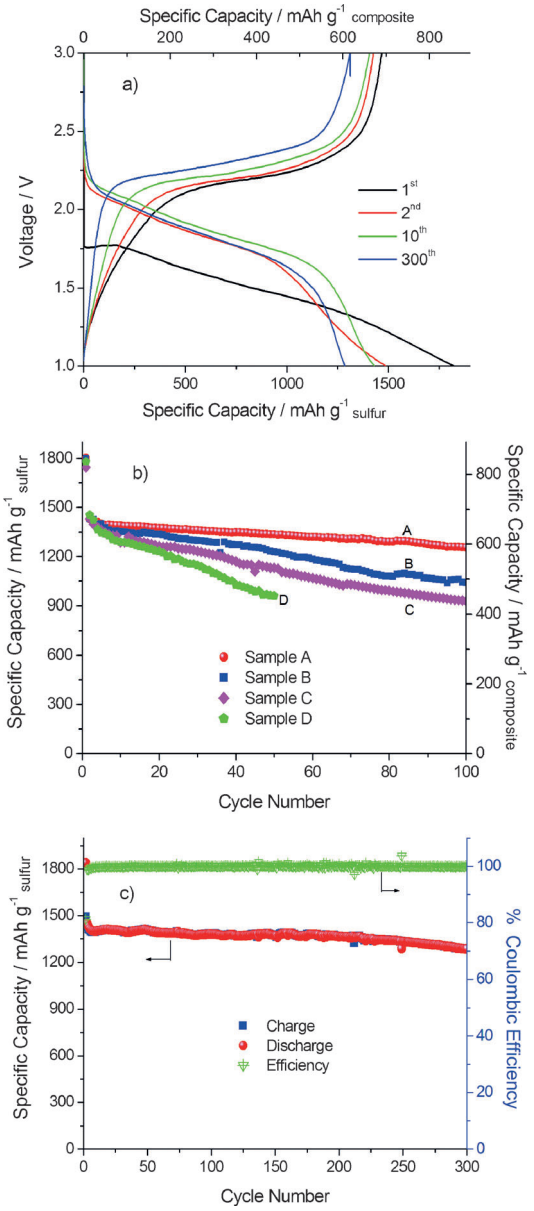

Figure 3. a) Typical discharge/charge curves of pPAN–S@GNS (sample A) versus lithium metal at 0.1 C rate; b) cycling performance of samples A–D at 0.1 C (1 C = 1672 mA g^{-1}_{sulfur}); c) cycling performance and Coulombic efficiency as a function of cycle number for sample A at 0.2 C.

Note that carbonates are the best known solvents for use in combination with pPAN–S composite cathode materials, performing better than ethers such as dimethoxyethane and 1,3-dioxolane. Ethers dissolve polysulfides, enhancing sulfur shuttling and, with age, causing gradual changes in active-material morphology and overall electrode structure, leading to poor Coulombic efficiency and rapid capacity fade. In some cases, carbonates have been found to be inappropriate for use in contact with elemental sulfur cathodes.[13] This point does not apply to pPAN–S composite cathode materials, however, which have been observed by a number of research groups to be stable in contact with carbonates.[14] The charge/discharge curves of pPAN–S composite cathode materials differ significantly from those obtained with elemental sulfur cathodes. There are no observable discharge plateaus, presumably owing to the complicated internal structure of the pPAN–S composite. We hypothesize that a solid solution, similar to an alloy, may form from the pPAN matrix and sulfur, which mainly exists in the form of smaller molecules such as S_4 and S_2—or even atomic sulfur—rather than S_8.[15] The detailed structure of pPAN–S composites and the mechanisms of carbonate–polysulfide interactions are still under investigation.

The capacity fades of composite samples A–D are compared in Figure 3b. The initial discharge capacities of the electrodes approach 1840 mAh g^{-1}_{sulfur}, exceeding the theoretical capacity of sulfur (1672 mAh g^{-1}_{sulfur}). This can be ascribed to the irreversible reaction of lithium with surface functional groups of the pPAN leading to lithium ion insertion into an anionic conjugated backbone, as is known to occur in conductive polymers.[16] The reversible capacities of the composites are approximately 1500 mAh g^{-1}_{sulfur} or approximately 700 mAh $g^{-1}_{composite}$ (calculated based on composite mass including pPAN and GNS) in the second cycle, corresponding to a sulfur utilization of approximately 90%. The capacity of sample D, which does not contain GNS, drops quickly with cycling; only around two thirds of the capacity is retained after 50 cycles. In contrast, samples B and C, which contain GNS, demonstrate fairly high reversibility. The hierarchically structured pPAN–S@GNS (sample A) produced by means of spray drying retains 88.8% of the initial reversible discharge capacity of 1449.3 mAh g^{-1}_{sulfur} after 300 cycles at a charge/discharge rate of 0.2 C. Also, as shown in Figure 3a and c, the columbic efficiencies (defined as the ratio of charge capacity to discharge capacity) approach 100%, except for in the first cycle (≈81%).

The discharge rate capabilities of samples A, C, and D were investigated and are illustrated in Figure 4a. A charge rate of 0.1 C was used during all cycling. The three materials demonstrate similar specific capacities at a discharge rate of 0.5 C, whereas sample A possesses significantly greater high-power rate capability than the other two samples. It delivers a capacity of approximately 700 mAh g^{-1}_{sulfur} even at 10 C—close to 50% of the initial reversible capacity. In contrast, samples C and D deliver comparable capacities at 6 C and 4 C, respectively. These results suggest that 3D GNS modification can effectively improve the rate performances of sulfur-containing composites.

Function of the graphene framework

The spherical graphene-wrapped pPAN–S@GNS composite described above has demonstrated high rate capability and excellent cycling stability. To rationalize in more detail the improved electrochemical performance observed after introducing GNS into a pPAN–S composite by spray drying, electronic conductivity and electrochemical impedance spectroscopy (EIS) measurements were performed on the pPAN–S@GNS and pPAN–S composites. The electronic conductivity of the former reaches 31 mS cm^{-1}, much higher than that of the latter (≈0.5 mS cm^{-1}). The considerably improved electronic transport derives from the superior electrical conductivity provided

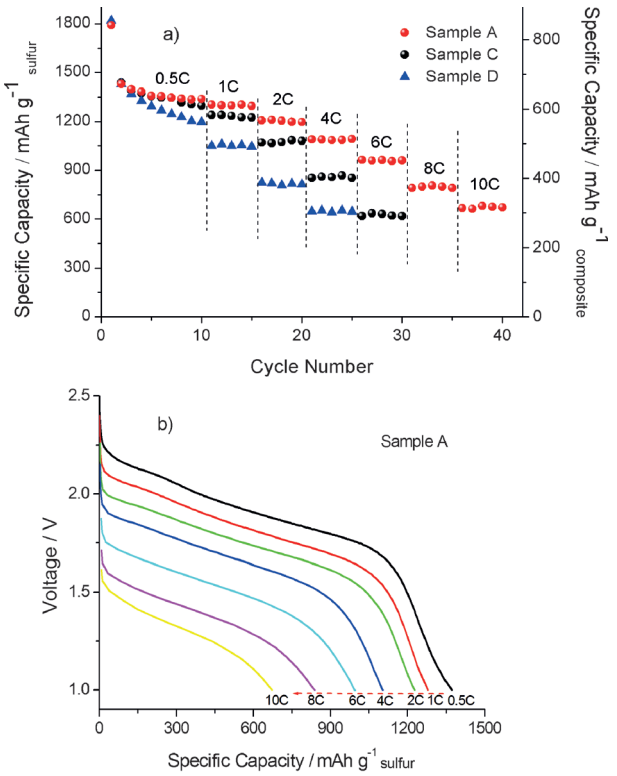

Figure 4. a) Power-rate performances of samples A, C, and D; b) discharge curves for sample A at various discharge rates.

by GNS. Table 1 shows that pPAN–S has a specific area of 15.36 $m^2 g^{-1}$, which doubles after GNS addition. pPAN–S is comprised of particles of approximately 100 nm in diameter with some aggregation, and pPAN–S@GNS composites are spheres with particle diameters of a few micrometers. To manifest an apparent area increase while the superficial particle size grows, abundant voids must exist in the pPAN–S@GNS microspheres. The Nyquist plot obtained from EIS of the pPAN–S@GNS also differs significantly from that of the pPAN–S (Figure 5). The shape of the depressed semicircle in the moderate-frequency region is determined by charge-transfer processes; the shape of the oblique feature at low frequencies is typically attributed to ion diffusion. The pPAN–S@GNS composite electrode (sample A) exhibits much lower and more stable charge-transfer resistance than the pPAN–S electrode (sample D), possibly because of the enhanced conductivity of the GNS and the rigid graphene-wrapped structure.

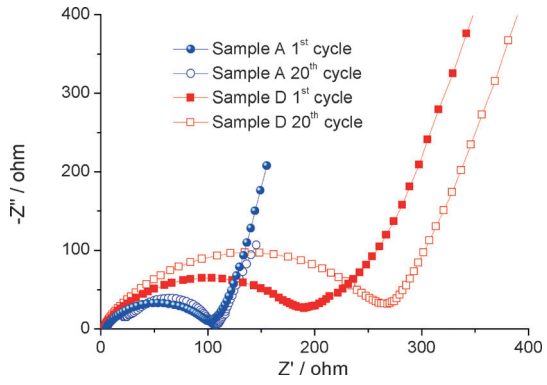

Figure 5. Impedance plots for electrodes of pPAN–S@GNS (sample A) and pPAN–S (sample D).

The morphology of composite sample A after long-term cycling is depicted in Figure 6. To minimize the effect on observed particle morphology, polytetrafluoroethylene (PTFE) was used as binder in the electrodes prepared for morphology studies. Although there is minimal change in the macroscopic morphology of pPAN–S@GNS after 100 cycles, the primary particles expand from approximately 100 nm to approximately 120 nm in diameter, as shown in the high magnification images. This observed variation is consistent with previous observations of extreme volume expansion within pPAN–S composite cathodes during cycling.[17] Also, the spherical skeleton surrounding the primary particles becomes less distinct after cycling than in the native material, possibly owing to interfacial reactions between carbonates and nucleophilic polysulfides—the discharge products of surface-absorbed sulfur. In the pPAN–S@GNS composite, GNS provides a 3D conductive matrix that is highly flexible and can accommodate the volume changes associated with discharge/charge processes.

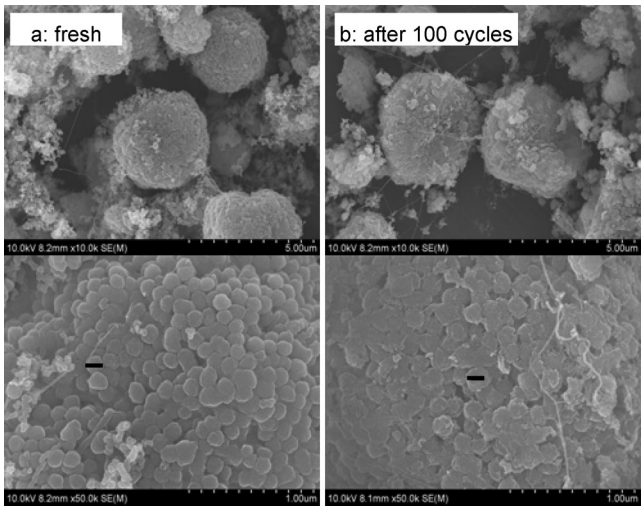

Figure 6. Morphology of pPAN–S@GNS (sample A) electrodes: a) fresh and b) after 100 cycles. 100 nm scale bars are superimposed on the bottom images for reference and show how the primary particles expand. The fibers are PTFE binder; the small nanoparticles (ca. 40 nm) are conductive carbon (Super P).

The improved electrochemical performance of the pPAN–S/GNS composite can be ascribed to three main factors: first, the porous hierarchical assembly of pPAN–S nanoparticles provides short paths for electrolyte diffusion; second, the GNS provides a support for monodisperse pPAN–S, hinders agglomeration and growth of the pPAN–S particles, and accommodates volume change during cycling; third, almost every pPAN–S particle maintains intimate contact with GNS, which works as a highly electronically conductive current collector throughout the composite material. In other words, continuous GNS layers

wrapped homogeneously around the surfaces of pPAN–S nanoparticles serve as fast paths for electron migration, and the voids in the secondary particles accommodate the electrolyte and facilitate Li-ion diffusion.

Conclusions

A spherical, hierarchically structured PAN@GNS composite is first synthesized by means of spray drying, and pPAN–S@GNS is prepared by subsequent heat treatment with elemental sulfur. The spray drying method is found to assemble PAN and GNS in such a manner that GNS loosely wrapped around the mono-disperse PAN nanoparticles. GNS inside the microspheres presumably integrate into a continuous conductive network, resulting in superior rate capability and excellent cycling stability for the pPAN–S@GNS composite material. The hierarchically microstructured pPAN–S@GNS composite demonstrates great promise for application as a high-performance cathode in next-generation rechargeable lithium-sulfur batteries. The ready availability of GNS and the high efficiency of spray drying facilitate scale-up of the provided synthesis for practical applications. In comparison to the previously reported pPAN–S/GNS sheets,[9] the pPAN–S@GNS microspheres developed here possess other clear advantages. These include the capability to improve interfacial stability, derived from the considerably reduced specific surface area of the secondary structure, spherical particle shapes, and higher tap density, all of which are key characteristics of electrode precursors sought by battery manufacturers.

Experimental Section

Materials synthesis: Acrylonitrile (AN) monomer (Aladdin) was washed with 3% phosphoric acid and with 5% sodium hydroxide to remove residual inhibitor, after which it was washed with distilled water, dried over calcium chloride, and stored in a refrigerator. Analytical grade S_8, potassium thiosulfate, sodium dodecyl sulfate (SDS), ammonia, and hydrazine hydrate (Aladdin), as well as commercial PAN (Aldrich), were used directly without further purification. GO was purchased from JCNANO.

GO was dispersed in water by ultrasonication using a Shangchao digital sonicator (FS-450, 450 W, 60% amplitude) for 30 min. Dispersed PAN nanoparticles were synthesized by dispersion/emulsion polymerization. Nanometer-sized PAN particles with an average diameter of 70 nm were formed by dissolving AN (6.2 mL), potassium thiosulfate (100 mg), and SDS (1.5 g) in water (93.8 mL). For the polymerization of AN, the vial was stirred at 70 °C for 10 h. The resulting particles were washed by centrifugation and subsequently dispersed in water by ultrasonication. The homogeneous GO/PAN dispersion (50 mL) was mixed with water (50 mL), hydrazine solution (50 μL, 35 wt% in water) and ammonia solution (350 μL, 28 wt% in water) in a 300 mL glass vial. After stirring vigorously for a few minutes, the vial was put in a water bath (95 °C) for 1 h. A combined suspension with PAN/GNS in a ratio of 10:1 by solution weight was spray dried at 220 °C using a BUCHI B-290 spray dryer to form solid PAN@GNS precursor for sample A. The precursor for sample B was prepared according to the above procedure except with commercial PAN; the precursor for sample C was prepared using common heat drying in place of spray drying. Sulfur-containing composites were prepared by heating the precursor mixtures with elemental sulfur in a nitrogen atmosphere. Sulfur content in the final composite depended on the amount added to the precursor, reaction temperature, and time. Typically, PAN@GNS (1.1 g) containing GNS (0.1 g) was mixed with elemental sulfur (7 g), heated at 300 °C, and kept for 6 h. There was approximately 0.9 g sulfur left in the composite, corresponding to a ratio of pPAN/GNS/S of 48:5:47 (wt%), as determined by elemental analysis. The pPAN–S composite without graphene (sample D) was synthesized by heating the mixture of PAN nanoparticles with sulfur under the conditions outlined above.

Structural characterization: Monomer conversion was determined gravimetrically. Elemental composition was measured by means of elemental analysis (Vario EL III elemental analyzer, Elementar). Morphologies and microstructures were characterized by using a SEM (Hitachi S-4800) and a TEM (JOEL JEM-100CX), respectively. XRD patterns were recorded by using CuK_α radiation at 40 kV with an X-ray diffractometer (D/max-220/PC, Rigaku). Specific surface areas were obtained by means of a Brunauer-Emmett-Teller (BET) surface area analyzer (ASAP 2010 M + C, Micrometrics Inc.). Electronic conductivities were measured by means of a four-point probe method (RTS-8 Four-Point probe meter).

Electrochemical measurements: Electrochemical performances of composites were evaluated using coin-type cells with lithium metal anodes. The cathode slurry comprised sulfur-containing composite, Super P conductive carbon black (40 nm, Timical) and polyvinylidene fluoride (PVDF) in *N*-methyl-2-pyrrolidone (NMP) at a weight ratio of 80:10:10. Carbon-coated Al was used for current collectors. For morphology studies, a different binder, PTFE, was used in the same proportion as PVDF/NMP. Sample electrodes with cathode loadings of approximately 2 mg cm^{-2}, corresponding to sulfur load ca. 0.752 mg cm^{-2}, were dried at 80 °C in vacuum for 12 h. The CR2016 coin cells were assembled in an argon-filled glove box (MBRAUN) using a conventional electrolyte of 1 M $LiPF_6$ in a mixture of ethylene carbonate and dimethyl carbonate (1:1 by volume), with a ENTEK ET20-26 separator. The charge and discharge tests were conducted with a LAND battery test system (Kingnuo) at 25 °C under constant current. The cut-off voltage range was 1–3 V vs. Li/Li$^+$. Electrochemical impedance spectroscopy (EIS) measurements were performed using a Solartron FRA 1250 frequency response analyzer in combination with a Solartron SI 1287 electrochemical interface, over the frequency range 100 kHz–0.1 Hz, with a signal amplitude of 5 mV.

Acknowledgements

This work was supported by the National Natural Science Foundation of China (51272156, 21333007, and 21273146) and a SJTU-UM joint research project.

Keywords: electrochemistry · graphene · nanostructures · rechargeable Li–S batteries · sulfur composite

[1] a) M. Winter, R. J. Brodd, *Chem. Rev.* **2004**, *104*, 4245 – 4269; b) J.-M. Tarascon, M. Armand, *Nature* **2001**, *414*, 359 – 367.

[2] a) P. G. Bruce, B. Scrosati, J.-M. Tarascon, *Angew. Chem.* **2008**, *120*, 2972 – 2989; *Angew. Chem. Int. Ed.* **2008**, *47*, 2930 – 2946; b) J. B. Goodenough, Y. Kim, *Chem. Mater.* **2010**, *22*, 587 – 603; c) B. Dunn, H. Kamath, J.-M. Tarascon, *Science* **2011**, *334*, 928 – 935; d) P. G. Bruce, S. A. Freunberger, L. J. Hardwick, J.-M. Tarascon, *Nat. Mater.* **2012**, *11*, 19 – 29.

[3] D. Peramunage, S. Licht, *Science* **1993**, *261*, 1029 – 1032.
[4] a) D. Marmorstein, T. H. Yu, K. A. Striebel, F. R. McLarnon, J. Hou, E. J. Cairns, *J. Power Sources* **2000**, *89*, 219 – 226; b) R. Rauh, F. Shuker, J. Marston, S. Brummer, *J. Inorg. Nucl. Chem.* **1977**, *39*, 1761 – 1766; c) K. Kang, Y. Meng, J. Breger, C. Grey, G. Ceder, *Science* **2006**, *311*, 977 – 980.
[5] a) X. G. Sun, X. Wang, R. T. Mayes, S. Dai, *ChemSusChem* **2012**, *5*, 2079 – 2085; b) G. Zheng, Y. Yang, J. J. Cha, S. S. Hong, Y. Cui, *Nano Lett.* **2011**, *11*, 4462 – 4467; c) J. Guo, Y. Xu, C. Wang, *Nano Lett.* **2011**, *11*, 4288 – 4294; d) X. Ji, K. Lee, L. Nazar, *Nat. Mater.* **2009**, *8*, 500 – 506; e) N. Jayaprakash, J. Shen, S. S. Moganty, A. Corona, L. A. Archer, *Angew. Chem.* **2011**, *123*, 6026 – 6030; *Angew. Chem. Int. Ed.* **2011**, *50*, 5904 – 5908; f) K. Cai, M. K. Song, E. J. Cairns, Y. Zhang, *Nano Lett.* **2012**, *12*, 6474 – 6479; g) R. Elazari, G. Salitra, A. Garsuch, A. Panchenko, D. Aurbach, *Adv. Mater.* **2011**, *23*, 5641 – 5644.
[6] a) L. Xiao, Y. Cao, J. Xiao, B. Schwenzer, M. H. Engelhard, L. V. Saraf, Z. Nie, G. J. Exarhos, J. Liu, *Adv. Mater.* **2012**, *24*, 1176 – 1181; b) X. Liang, Z. Wen, Y. Liu, H. Zhang, J. Jin, M. Wu, X. Wu, *J. Power Sources* **2012**, *206*, 409 – 413; c) F. Wu, J. Chen, R. Chen, S. Wu, L. Li, S. Chen, T. Zhao, *J. Phys. Chem. C* **2011**, *115*, 6057 – 6063.
[7] a) J. Wang, J. Yang, J. Xie, N. Xu, *Adv. Mater.* **2002**, *14*, 963 – 965; b) Y. Zhang, Y. Zhao, A. Yermukhambetova, Z. Bakenov, P. Chen, *J. Mater. Chem. A* **2013**, *1*, 295 – 301; c) J. Guo, Z. Yang, Y. Yu, H. D. Abruna, L. A. Archer, *J. Am. Chem. Soc.* **2013**, *135*, 763 – 767.
[8] a) G. Li, G. Li, S. Ye, X. Gao, *Adv. Energy Mater.* **2012**, *2*, 1238 – 1245; b) K. T. Lee, R. Black, T. Yim, X. Ji, L. F. Nazar, *Adv. Energy Mater.* **2012**, *2*, 1490 – 1496; c) Z. W. Seh, W. Li, J. Cha, G. Zheng, Y. Yang, M. T. McDowell, P. C. Hsu, Y. Cui, *Nat. Commun.* **2013**, *4*, 1331.
[9] L. Yin, J. Wang, F. Lin, J. Yang, Y. Nuli, *Energy Environ. Sci.* **2012**, *5*, 6966 – 6972.
[10] a) Y. Chen, F. Guo, A. Jachak, S.-P. Kim, D. Datta, J. Liu, I. Kulaots, C. Vaslet, H. D. Jang, J. Huang, A. Kane, V. B. Shenoy, R. H. Hurt, *Nano Lett.* **2012**, *12*, 1996 – 2002; b) J. Luo, H. D. Jang, T. Sun, L. Xiao, Z. He, A. P. Katsoulidis, M. G. Kanatzidis, J. M. Gibson, J. Huang, *ACS Nano* **2011**, *5*, 8943 – 8949; c) X. Ma, M. R. Zachariah, C. D. Zangmeister, *Nano Lett.* **2012**, *12*, 486 – 489; d) M. Zhu, P. Chen, M. Liu, *ACS Nano* **2011**, *5*, 4529 – 4536; e) S. Yang, X. Feng, S. Ivanovici, K. Müllen, *Angew. Chem.* **2010**, *122*, 8586 – 8589; *Angew. Chem. Int. Ed.* **2010**, *49*, 8408 – 8411.
[11] D. Li, M. B. Muller, S. Gilje, R. B. Kaner, G. G. Wallace, *Nat. Nanotechnol.* **2008**, *3*, 101 – 105.
[12] L. Boguslavsky, S. Baruch, S. Margel, *J. Colloid Interface Sci.* **2005**, *289*, 71 – 85.
[13] J. Gao, M. A. Lowe, Y. Kiya, H. D. Abruna, *J. Phys. Chem. C* **2011**, *115*, 25132 – 25137.
[14] a) K. Jeddi, M. Ghaznavi, P. Chen, *J. Mater. Chem. A* **2013**, *1*, 2769 – 2772; b) C. Lai, X. P. Gao, B. Zhang, T. Y. Yan, Z. Zhou, *J. Phys. Chem. C* **2009**, *113*, 4712 – 4716; c) J. Fanous, M. Wegner, J. Grimminger, Ä. Andresen, M. R. Buchmeiser, *Chem. Mater.* **2011**, *23*, 5024 – 5028.
[15] a) J. Wang, Z. Yao, C. W. Monroe, J. Yang, Y. Nuli, *Adv. Funct. Mater.* **2013**, *23*, 1194 – 1201; b) S. Xin, L. Gu, N. Zhao, Y. Yin, L. Zhou, Y. Guo, L. Wan, *J. Am. Chem. Soc.* **2012**, *134*, 18510 – 18513.
[16] a) T. F. Otero, I. Cantero, *J. Power Sources* **1999**, *81 – 82*, 838 – 841; b) A. G. MacDiarmid, *Angew. Chem.* **2001**, *113*, 2649 – 2659; *Angew. Chem. Int. Ed.* **2001**, *40*, 2581 – 2590.
[17] X. He, J. Ren, L. Wang, W. Pu, C. Jiang, C. Wan, *J. Power Sources* **2009**, *190*, 154 – 156.

Received: July 23, 2013
Revised: September 15, 2013
Published online on October 23, 2013